A study of the $A^2\Pi$–$X^2\Sigma^+$ and $B^2\Sigma^+$–$X^2\Sigma^+$ band systems of scandium monosulfide, ScS, using Fourier transform emission spectroscopy and laser excitation spectroscopy

Jamie Gengler [a], Jinhai Chen [a], T.C. Steimle [a,*], R.S. Ram [b], P.F. Bernath [c]

[a] Department of Chemistry and Biochemistry, Arizona State University, Tempe, AZ 85287-1604, USA
[b] Department of Chemistry, University of Arizona, Tucson, AZ 85721, USA
[c] Department of Chemistry, University of Waterloo, Waterloo, Ont., Canada N2L 3G1

Abstract

Emission spectra of the $A^2\Pi_{3/2}$–$X^2\Sigma^+$ (0, 1), (0, 0), and (1, 0) bands and the $B^2\Sigma^+$–$X^2\Sigma^+$ (0, 1), (0, 0), (1, 0), (2, 0), and (3, 1) bands of ScS have been recorded in the 10 000–13 500 cm^{-1} region at a resolution of 0.05 cm^{-1} using a Fourier transform (FT) spectrometer. The $A^2\Pi_r$–$X^2\Sigma^+$ (1, 0) band as well as the $B^2\Sigma^+$–$X^2\Sigma^+$ (0, 0) and (1, 0) bands have been recorded at high resolution (± 0.001 cm^{-1}) by laser excitation spectroscopy using a supersonic molecular beam source. The FT spectral features range up to $N = 148$, while those recorded with the laser cover the "low-N" regions. The lines recorded with the laser exhibit splittings due to the ^{45}Sc ($I = 7/2$) magnetic hyperfine interactions, which are large (~ 6.65 GHz) in the $X^2\Sigma^+$ state and much smaller in the $B^2\Sigma^+$ and $A^2\Pi$ states. The energy levels were modeled using a traditional 'effective' Hamiltonian approach, and improved spectroscopic constants were extracted and compared with previous determinations and theoretical predictions.
© 2006 Elsevier Inc. All rights reserved.

Keywords: Scandium monosulfide; Fourier transform emission; Laser excitation spectroscopy

1. Introduction

Transition metal-containing molecules are species of chemical and astrophysical importance. Diatomic molecules like ScS are simple transition metal-containing systems in which d-electrons take part in bonding, and they provide ideal models for the understanding of electronic structure and reactivity. The limited number of valence electrons, small spin–orbit interaction, and single isotope (^{45}Sc with $I = 7/2$), make scandium-containing molecules attractive for theoretical and experimental studies of transition metal chemistry. Bonding and electronic structure information can best be gleaned from comparative studies of isovalent scandium-containing molecules such as scandi-um monoxide, ScO, and scandium monosulfide, ScS. These two species have intense visible band systems that to a first approximation represent a $4s(\sigma) \rightarrow 3d_{\pm 1}/4p_{\pm 1}(\pi)$ ($A^2\Pi$-$X^2\Sigma^+$) and $4s(\sigma) \rightarrow 3d_0/4p_0(\sigma)$ ($B^2\Sigma^+$–$X^2\Sigma^+$) promotion [1]. The principal difference between these two molecules lies in the longer and weaker ScS bond [2]. Spectroscopy of transition metal-containing sulfides are also of astrophysical importance, as TiS [3] and ZrS [4] have been tentatively identified in S-type Mira variable stars, and there is strong possibility that other transition metal sulfides such as ScS may also be found. Precise spectroscopic data are necessary for a search for these species in complex stellar spectra.

So far only limited spectroscopic data are available for ScS. Although the $A^2\Pi$–$X^2\Sigma^+$ and $B^2\Sigma^+$–$X^2\Sigma^+$ band systems have been known for several decades [5,6], the spectra of ScS are much less studied than those of ScO. These ScS transitions, which are shifted to the red relative to those of

ScO, were recorded at near Doppler resolution using conventional emission spectroscopy [5]. The $B^2\Sigma^+$–$X^2\Sigma^+$ (0,0) band was analyzed [6] to produce a set of fine and hyperfine parameters. A liquid nitrogen-cooled hollow cathode discharge source was used, but the low-N lines were not assigned.

Recently the permanent electric dipole moments of the $(v = 1)$ $B^2\Sigma^+$ and $(v = 0)$ $X^2\Sigma^+$ states were determined from the analysis of the molecular beam optical Stark laser excitation spectra [also called laser induced fluorescence (LIF)] for numerous lines of the $B^2\Sigma^+$–$X^2\Sigma^+$ (1,0) band [7]. The $(v = 1)$ $B^2\Sigma^+$ state in [7] was erroneously referred to as the $(v = 0)$ $B^2\Sigma^+$ state. A prerequisite for the analysis of the optical Stark spectra was the recording and analysis of the field-free low-N lines of the $B^2\Sigma^+$–$X^2\Sigma^+$ (1,0) band. Only lines having $N'' \leqslant 3$ were included in the analysis. A review of the spectroscopy can be found in [7].

Here, we report on the observation of emission spectra of the $A^2\Pi_{3/2}$–$X^2\Sigma^+$ (0,1), (0,0), and (1,0) bands as well as the $B^2\Sigma^+$–$X^2\Sigma^+$ (0,1), (0,0), (1,0), (2,0), and (3,1) bands using Fourier transform (FT) spectroscopy. We also report on the observation of the $A^2\Pi_r$–$X^2\Sigma^+$ (1,0) band as well as the $B^2\Sigma^+$–$X^2\Sigma^+$ (0,0) and (1,0) bands using molecular beam LIF spectroscopy. A total of 4159 lines were combined in a weighted least squares fit to produce an improved set of spectroscopic parameters for the $B^2\Sigma^+$, $X^2\Sigma^+$, and $A^2\Pi$ states.

2. Experimental

2.1. Fourier transform emission spectroscopy

The FTS emission bands of ScS were observed inadvertently in an experiment intended to search for TiH bands using a commercial high temperature carbon tube furnace. The experiment was intended to produce the TiH bands from the reaction of Ti metal vapor with 160 Torr of H_2 at a temperature of about 2150 °C. In addition to H_2, about 100 Torr of He was also present in the furnace to serve as a buffer gas. The observed spectra were full of bands of the electronic transitions of TiO, TiS, ScF, and ScS. The scandium metal required to produce the Sc-containing molecules was present in the furnace from a previous experiment. The sulfur impurities necessary to make ScS were also present in the furnace from previous metal sulfide experiments.

The spectra in the 8500–16 000 cm^{-1} interval were recorded with the 1-m Fourier transform spectrometer associated with the McMath-Pierce telescope of the National Solar Observatory at Kitt Peak. The spectrometer was equipped with a UV beamsplitter, RG645 red pass filters and midrange silicon diode detectors. The spectra were recorded by co-adding 4 scans in about 45 min of integration at a resolution of 0.05 cm^{-1}. The spectral line positions were determined using a data reduction program called PC-DECOMP developed by Brault. The peak positions were determined by fitting a Voigt lineshape function

to each line. The ScS rotational lines were observed with a typical signal-to-noise ratio of 5:1 and have an approximate linewidth of 0.110 cm^{-1}. The rotational lines were calibrated using the measurements of TiO bands [8] also observed in the same spectra, and the measurements are expected to have an accuracy of ±0.007 to ±0.01 cm^{-1} depending upon the signal-to-noise ratio and extent of blending.

2.2. Supersonic molecular beam laser spectroscopy

The LIF measurements of the $A^2\Pi$–$X^2\Sigma^+$ (1,0), $B^2\Sigma^+$–$X^2\Sigma^+$ (0,0), and $B^2\Sigma^+$–$X^2\Sigma^+$ (1,0) bands were performed at Arizona State University. A modified version of the laser ablation/supersonic expansion production scheme used in the previous ScS study [7] was selected for sample preparation. A variable speed rotating Sc metal rod was irradiated by the third harmonic (355 nm) light originating from a Q-switched Nd:YAG laser operating at approximately 1 mJ/pulse and at 20 Hz. Argon gas at a backing pressure of about 2000 kPa flowed over a room temperature sample of carbon disulfide. A commercial solenoid type valve was used to introduce this gas mixture into a nozzle assembly for reaction with the laser-vaporized metal. A 5-mm diameter skimmer, situated approximately 15 cm downstream from the ablation source, separated the two compartments of the differentially pumped chambers of the molecular beam apparatus. Typical operating pressures of approximately 5×10^{-5} and 1×10^{-6} Torr for the source and detection chambers, respectively, were maintained.

The LIF spectra were recorded using a stabilized, single longitudinal mode, continuous wave Ti:sapphire ring laser. Approximately 50 mW of loosely focused laser radiation intersected the molecular beam sample at a 90° angle 10 cm downstream from the skimmer. The resulting LIF was collected and collimated with a lens assembly and directed through a ±10 nm band-pass filter centered at the excitation wavelength. The filtered LIF signal was detected via a cooled photomultiplier tube and processed using gated single-photon counting techniques.

Wavelength calibration of the $B^2\Sigma^+$–$X^2\Sigma^+$ (0,0) $(T_{00} = 12455.7738$ cm$^{-1})$ and $B^2\Sigma^+$–$X^2\Sigma^+$ (1,0)$(T_{10} = 12940.3981$ cm$^{-1})$ spectra utilized a heated I_2 cell and the published transition wavenumbers of Gerstenkorn and Luc [9]. The wavelength of the $A^2\Pi$–$X^2\Sigma^+$ (1,0) band system is too red $(T_{10} = 11571.4218$ cm$^{-1})$ for convenient use of the I_2 calibration scheme and a uranium optogalvanic cell was used for calibration. The atomic transition wavenumbers were taken from the Los Alamos atlas [10]. The experimental arrangement described by Sansonetti and Weber [11] was employed. Simultaneous recording of the transmission of two confocal étalons assisted in the required long wavenumber extrapolation from the uranium calibration lines to the ScS LIF features. One étalon, 10 cm in length and thoroughly described in a previous paper [12], was temperature controlled, evacuated, and actively stabilized by monitoring the transmission of a frequency

stabilized He–Ne laser. The free spectral range (FSR) was accurately determined to be 753.58 MHz by measuring the spacing between two features in the electronic spectrum of titanium monoxide [12]. A second, unstabilized, 1 m confocal étalon (FSR = 75 MHz) was used to extrapolate between transmission peaks of the 10-cm, stabilized, confocal étalon.

3. Observations

The low rotational energy levels of the $X^2\Sigma^+$, $A^2\Pi$, and $B^2\Sigma^+$ states exhibit a pattern typical of a molecule near the Hund's *case* $b_{\beta S}$, *case* $a_{\beta J}$ and *case* $b_{\beta J}$ coupling scheme limits, respectively. The approximately good intermediate quantum number for the *case* $b_{\beta S}$ $X^2\Sigma^+$ state is G ($\mathbf{G} = \mathbf{I} + \mathbf{S}$) and each rotational level is split into a pair (G-doubling) due to the strong coupling of the ^{45}Sc ($I = 7/2$) nuclear spin with the electronic spin through the Fermi contact interaction. G is equal to 3 for the lower level and 4 for the upper level of each doublet because the Fermi contact parameter (b_F) in the $X^2\Sigma^+$ state is positive, and the nuclear g-factor of ^{45}Sc is positive [13]. The electronic spin decouples from the nuclear spin and couples to the nuclear frame rotation with increasing rotation due to spin–rotation interaction. This recoupling causes each degenerate $G = 3$ and 4 set of levels to split into two groups of $2G + 1$ (=7 and 9) components that are characterized by the total angular momentum quantum number $F(\mathbf{F} = \mathbf{G} + \mathbf{N})$. At very high rotational excitation the energy level pattern of the $X^2\Sigma^+$ state approaches the Hund's *case* $b_{\beta J}$ limit so that the two groups of $2G + 1$ F levels at lower N have transformed to two groups of $2I + 1$ (=8) F levels and J ($\mathbf{J} = \mathbf{N} + \mathbf{S}$) becomes the approximately good intermediate quantum number. In other words at high N, the more usual pattern appears with each rotational level (N) doubled into two (electron) spin components (J), which are each split into eight hyperfine components (F). At low N, however, because the Fermi contact hyperfine interaction is bigger than the spin–rotation interaction, the observed doubling is a hyperfine doubling (G) and not the more usual electron spin doubling typically seen in $^2\Sigma^+$ states.

Unlike the $X^2\Sigma^+$ state, the magnetic hyperfine interaction in the $B^2\Sigma^+$ state is relatively small compared to the spin–rotation interaction making the energy level pattern that of a molecule near the *case* $b_{\beta J}$ limit. The $B^2\Sigma^+$ state thus has a typical $^2\Sigma^+$ energy level pattern with J the appropriate intermediate quantum number for both the low and high rotational levels.

The rotational energy level pattern for low to moderate rotational levels of the $A^2\Pi$ state is near the *case* $a_{\beta J}$ limit because the spin–orbit interaction is large compared to the rotational energy spacing, which in turn is large compared to the magnetic hyperfine interaction. Each rotational level of the $A^2\Pi_{3/2}$ and $A^2\Pi_{1/2}$ spin–orbit components consists of a Λ-doublet characterized by the intermediate quantum number J. The Λ-doubling is large in the $A^2\Pi_{1/2}$ spin component and increases approximately linearly with J, but is nearly negligible in the $A^2\Pi_{3/2}$ spin component. Each Λ-doublet is composed of a nearly degenerate set of hyperfine split levels whose total angular momentum quantum number, F ($\mathbf{F} = \mathbf{J} + \mathbf{I}$), is given by the usual vector coupling of $\mathbf{J}$ and $\mathbf{I}$. At very high rotational excitation the pattern would transform to the *case* $b_{\beta J}$ limit by electron spin uncoupling.

There are sixteen branches in a $^2\Pi$ (*case* $a_{\beta J}$)–$^2\Sigma^+$ (*case* $b_{\beta S}$) band and eight branches for a $^2\Sigma^+$ (*case* $b_{\beta J}$)–$^2\Sigma^+$ (*case* $b_{\beta S}$) band. The branch designation used here for the $A^2\Pi$–$X^2\Sigma^+$ band system is a modified version of the conventional $^2\Pi$ (*case* $a_{\beta J}$)–$^2\Sigma^+$ (*case* $b_{\beta J}$) labeling scheme with $^{\Delta N}\Delta J_{F'_i F''_i}(N'')$ in which the second subscript "F''_i" ($i = 1$ or 2 for $J = N + 1/2$ or $N - 1/2$) is replaced by the intermediate good quantum number G for the $X^2\Sigma^+$ state. The same branch-labeling scheme was used for ScO [14]. The LIF data for the $A^2\Pi$–$X^2\Sigma^+$ band consists of all 16 expected branches while the FT emission data for the $A^2\Pi_{3/2}$–$X^2\Sigma^+$ sub-bands consists of the $^PP_{23}$, $^QP_{23} + ^QQ_{23}$, $^QP_{24} + ^QQ_{24}$, $^RQ_{23} + ^RR_{23}$, $^RQ_{24} + ^RR_{24}$, and $^SR_{24}$ branches. The LIF data for the $B^2\Sigma^+$–$X^2\Sigma^+$ bands consists of all eight expected branches while the FT emission data, for which the *case* $b_{\beta S}$ to *case* $b_{\beta J}$ transformation of the $X^2\Sigma^+$ state has occurred at high rotational excitation, has only the $^PP_{23}$, $^RQ_{23} + ^RR_{23}$, $^RQ_{14} + ^RR_{14}$, and $^PP_{14} + ^PQ_{14}$ branches. The $^RQ_{24} + ^RR_{24}$ and $^PP_{13} + ^PQ_{13}$ branches are too weak to be detected because they correspond to $\Delta N \neq \Delta J$ transitions [15].

A total of 4159 lines were observed with 2619 from the FT experiments and 1540 from the LIF experiments. A representative portion of the high-resolution LIF spectra in the region of the $A^2\Pi_{1/2}$–$X^2\Sigma^+$ (1,0) band is presented in Fig. 1. Twenty ablation pulses at a given excitation wavelength were co-added for all LIF spectra. The F' and F'' assignment for each transition is also given, with only the low F values indicated for clarity. All features in the spectrum can be assigned. The lines labeled $^OP_{14}(2)$ and $^OP_{13}(2)$ both consist of two groups of hyperfine components separated by 1.5 GHz, reflecting the $F = 3$–4 hyperfine splitting of the common $J = 1/2$ f-parity upper level, while the 6.65 GHz separation between them is the ground state $G = 3$–4 splitting. The fine splitting of $\sim$30 MHz evident in the $^OP_{14}(2)$ and $^OP_{13}(2)$ features is the lifting of the degeneracy of the G-levels as $\mathbf{I}$ and $\mathbf{S}$ decouple in the $X^2\Sigma^+$ state. For the $^OP_{14}(2)$ feature there are a total of six resolvable hyperfine components, while for the $^OP_{13}(2)$ feature there are only five. The $F' = 4$-$F'' = 4$ component for the $^OP_{13}(2)$ feature is not resolved from the more intense $F' = 4$-$F'' = 5$ component and therefore was not independently labeled or used in the analysis. The quantum number assignments for all observed transitions, as well as the observed minus calculated values, are listed in the supplemental material to this paper [16]. Also presented in Fig. 1 is the predicted spectrum obtained using the optimized set of spectroscopic parameters, a temperature of 40 K and 30 MHz full width at half maximum (FWHM)
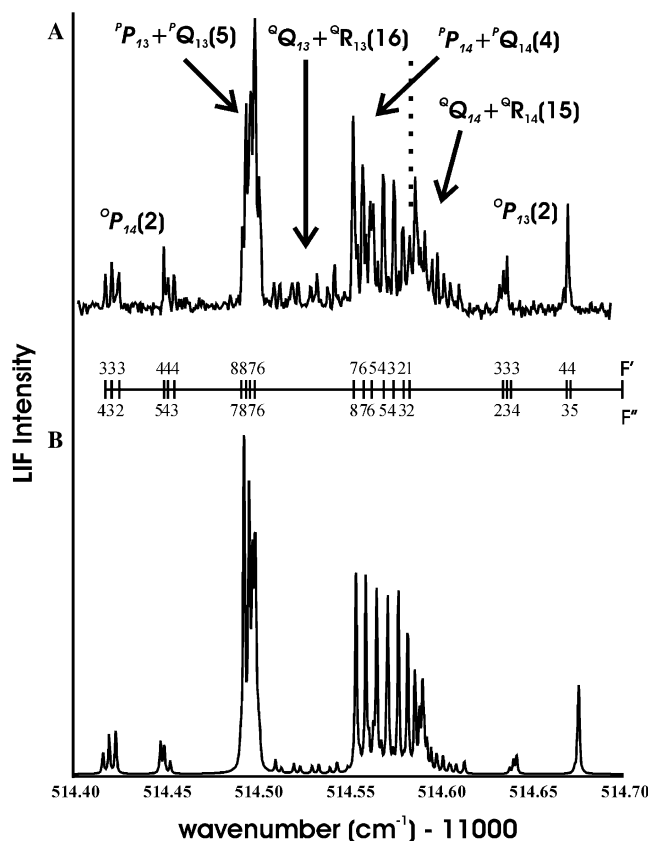
Fig. 1. A representative portion of the (A) experimental LIF spectra, and (B) calculated spectra of the $(1,0)$ band of the $A^2\Pi_{3/2}–X^2\Sigma^+$ transition of ScS.

Fig. 2. A portion of the FT spectra of the $A^2\Pi_{3/2}–X^2\Sigma^+$ $(0,0)$ band of ScS near the R-heads.

Lorentzian lineshape. Details of the prediction procedure for all the bands are given below.

The FT spectra are complex because of overlapping from the spectra of other species such as TiO, TiS, and ScF, as mentioned earlier. The bands of the $A^2\Pi–X^2\Sigma^+$ system of ScS are badly overlapped by the strong $C^3\Delta–X^3\Delta$ bands of TiS. Although the rotational lines belonging to the $A^2\Pi_{1/2}–X^2\Sigma^+$ bands could not be measured with good precision, we were able to measure and assign lines belonging to the $(0,1)$, $(0,0)$ and $(1,0)$ bands of the $A^2\Pi_{3/2}–X^2\Sigma^+$ transition. A part of the spectrum of the $(0,0)$ band of the $A^2\Pi_{3/2}–X^2\Sigma^+$ transition is provided in Fig. 2. To avoid confusion, we have marked only the band head positions in Fig. 2. At first glance it is difficult to find the pattern of branches because of frequent overlapping of the different branches. A color Loomis-Wood program running on a PC was very helpful in sorting out the branches. Rotational lines up to $N'' = 119$ were identified in the $(0,0)$ band.

Representative portions of the high-resolution LIF spectra in the region of the $B^2\Sigma^+–X^2\Sigma^+$ $(1,0)$ band system are presented in Fig. 3. The left half of this figure shows part of the P branch, while the right half shows part of the overlapping Q and R branches. The predicted spectra are also given for comparison. The $^RQ_{23} + {}^RR_{23}(2)$ and $^RR_{14}(4)$ lines are congested because the effects of the hyperfine splitting in the $B^2\Sigma^+$ state nearly cancel the
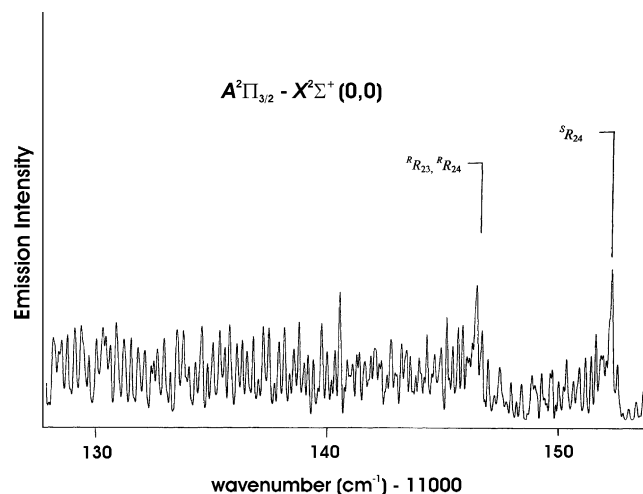
effects of the spin uncoupling in the $X^2\Sigma^+$ state. There are discrepancies between the observed and predicted spectra of Fig. 3. Most notable is that the $^PP_{13} + {}^PQ_{13}(5)$ feature and the $^RR_{13}(3)$ feature, which is overlapped by the $^RR_{14}(4)$ line, are observed approximately 0.01 cm^{-1} higher than predicted. The observed transition wavenumber for the $^RR_{14}(3)$ feature (not shown) also exhibits a similar deviation. All three lines have the F_1 $(J = 4.5)$ component of the $N = 4$ level in the $B^2\Sigma^+$ $(v = 1)$ state as the upper state. The $^PP_{14} + {}^PQ_{14}(5)$ line, which also has the same upper state, was not recorded. A second, less striking, discrepancy is that the observed $^RR_{14}(4)$ line is shifted approximately 0.003 cm^{-1} lower than predicted. The $^RR_{13}(4)$ feature (not shown), which shares the same upper state level, is also observed to show a similar $(\approx 0.005$ cm$^{-1})$ shift. These transitions have the F_1 component of the $N = 5$ level in the $B^2\Sigma^+$ $(v = 1)$ state as the upper state. No other lines sharing this upper energy level were recorded. It is concluded that the F_1 component of $N = 4$ and to a lesser extent the F_1 component of the $N = 5$ rotational level in the $B^2\Sigma^+$ $(v = 1)$ state exhibit small local perturbations.

In the present study 671 features of the $B^2\Sigma^+–X^2\Sigma^+$ $(1,0)$ band have been measured as compared to only 56 in the previous study [7]. The quality of the spectra recorded here is far superior to what was previously recorded as part of the optical Stark study [7] because of an improved S/N ratio and improvements made in wavelength calibration. The newly measured transition wavenumbers differ significantly from those given in [7] and a few of the weaker features were re-assigned.

A portion of the $B^2\Sigma^+–X^2\Sigma^+$ $(0,0)$ band observed in the FT spectra is provided in Fig. 4 in which we have marked the positions of the R branch band heads. The rotational lines in the different branches were again identified using a Loomis-Wood program. Only the $^PP_{14} + {}^PQ_{14}$, $^RQ_{23} + {}^RR_{23}$, $^PP_{23}$, and $^RR_{14}$ branches were identified in
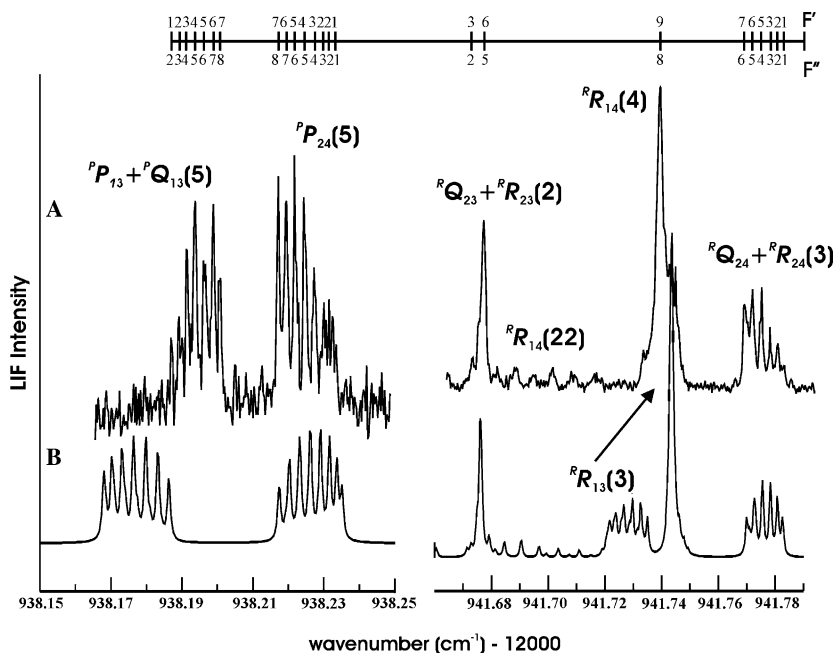
Fig. 3. A representative portion of the (A) experimental LIF spectra, and (B) calculated spectra of the $B^2\Sigma^+$-$X^2\Sigma^+$ (1,0) band of ScS.
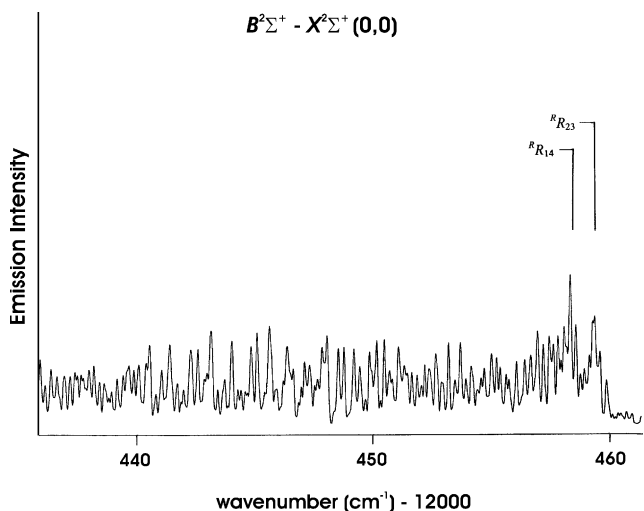

Fig. 4. A portion of the FT spectra of the $B^2\Sigma^+$–$X^2\Sigma^+$ (0,0) band of ScS near the R-heads.

the bands of the $B^2\Sigma^+$–$X^2\Sigma^+$ transition unlike in the laser spectra. Rotational assignments were made by comparing the combination differences of common vibrational levels.

Although very high N rotational lines were observed in the FT spectra because of the high temperature of the furnace, the low N lines were not identified because of spectral congestion in the band head region. The low N rotational lines were measured using the LIF spectra. Representative portions of the high-resolution LIF spectra in the region of the $B^2\Sigma^+$–$X^2\Sigma^+$ (0,0) band are presented in Fig. 5 along with the predicted spectra. This figure shows the same low N spectral features as those in Fig. 3. The predictions

are now in excellent agreement with the observations confirming that the $B^2\Sigma^+$–$X^2\Sigma^+$ (1,0) band must be slightly perturbed. The $^R R_{14}(22)$ feature seen in Fig. 3 is not seen in Fig. 5 because the slight difference in spectroscopic parameters for the $B^2\Sigma^+$ ($v = 1$) state compared to the $B^2\Sigma^+$ ($v = 0$) state shifts this feature outside the spectral region displayed in Fig. 5. The intensity patterns of the observed and calculated spectra are also in better agreement for the $B^2\Sigma^+$–$X^2\Sigma^+$ (0,0) band than for the $B^2\Sigma^+$–$X^2\Sigma^+$ (1,0) band.

A portion of the high N region of the spectrum of the $B^2\Sigma^+$–$X^2\Sigma^+$ (3,1) band is provided in Fig. 6, and a number of rotational lines in the $^R Q_{23} + {}^R R_{23}$, $^P P_{23}$, and $^P P_{14} + {}^P Q_{14}$ branches have been marked. Although this band is much weaker than the other bands, lines up to $N'' = 106$ could be identified. In comparing the data obtained by the King furnace/FT and molecular beam/LIF experiments, two primary differences should be noted. First, only the $A^2\Pi_{3/2}$–$X^2\Sigma^+$ sub-bands were observed by the King furnace/FT method due to strong overlapping by lines originating from the TiS contaminant. Second, as noted above, not all of the branches seen in the molecular beam/LIF data survive at high N values, as seen in the King furnace/FT data.

4. Analysis

A direct fit to the transition wavenumbers was made analogous to that performed earlier for ScS [7] and LaO [17]. The fine and hyperfine effects in the $X^2\Sigma^+$ and $B^2\Sigma^+$ states were modeled by including the rotation, spin–rotation, magnetic hyperfine and electric quadrupole interactions [18]:
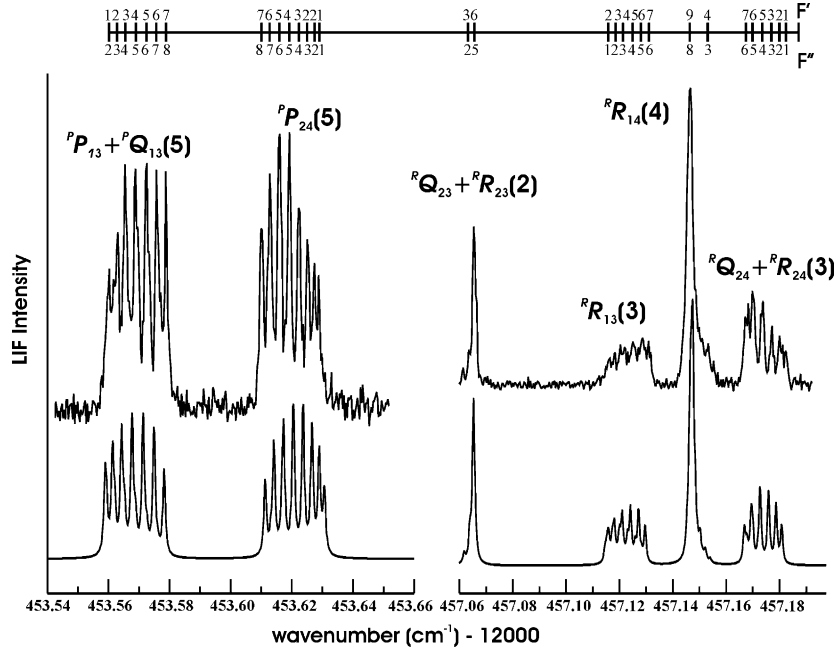
Fig. 5. A representative portion of the LIF as well as predicted spectra of the $B^2\Sigma^+$–$X^2\Sigma^+$ (0,0) band of ScS.
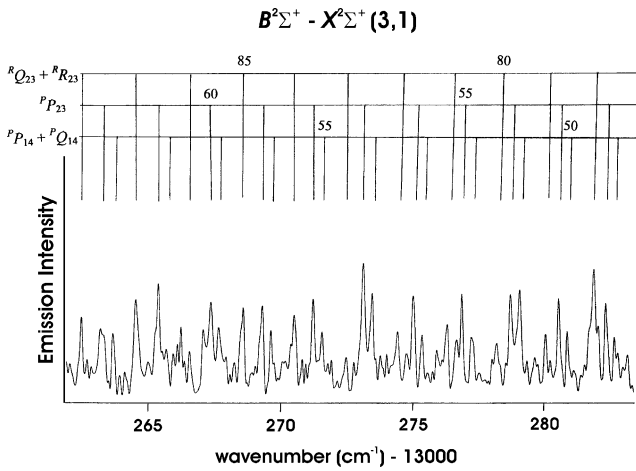

Fig. 6. An expanded portion of the FT spectra of the (3,1) band of the $B^2\Sigma^+$–$X^2\Sigma^+$ transition of ScS, with some high N rotational lines marked.

$$\mathbf{H}^{\mathrm{eff}}(X, B^2\Sigma^+) = T_v + B\mathbf{N}^2 - D\mathbf{N}^4 + \gamma\mathbf{N}\cdot\mathbf{S}$$
$$+ \gamma_D\tfrac{1}{2}[\mathbf{N}\cdot\mathbf{S}, \mathbf{N}^2]_+ + b_F\mathbf{I}\cdot\mathbf{S}$$
$$+ c(I_zS_z - \tfrac{1}{3}\mathbf{I}\cdot\mathbf{S})$$
$$+ \frac{eq_0Q}{4I(2I-1)}(3I_z^2 - \mathbf{I}^2), \tag{1}$$

In Eq. (1), $\mathbf{N}$ is the angular momentum operator excluding electronic and nuclear spin, $\mathbf{S}$ and $\mathbf{I}$, respectively, and $[\mathbf{N}\cdot\mathbf{S}, \mathbf{N}^2]_+$ is the anticommutator of the $\mathbf{N}\cdot\mathbf{S}$ and $\mathbf{N}^2$ operators. A 16×16 matrix representation, constructed using a case $a_{\beta J}$, non-parity, basis set, $\Psi = |n\Lambda; S\Sigma; J\Omega; IFM_F\rangle$, was numerically diagonalized to produce the eigenvalues and eigenvectors. The fine and hyperfine effects in the $A^2\Pi$ state were modeled by including the spin-orbit, rotation,

Λ-doubling interaction terms, and magnetic hyperfine interactions [18]:

$$\mathbf{H}^{\mathrm{eff}}(A^2\Pi) = T_v + AL_zS_z + \tfrac{1}{2}A_D[\mathbf{N}^2, L_zS_z]_+ + B\mathbf{N}^2 - D\mathbf{N}^4$$
$$+ \tfrac{1}{2}(p+2q)(e^{2i\varphi}S_-J_- + e^{-2i\varphi}S_+J_+)$$
$$- \tfrac{1}{2}q(e^{2i\varphi}J_-^2 + e^{-2i\varphi}J_+^2) + aI_zL_z$$
$$- \tfrac{1}{2}d(S_+I_+ + S_-I_-). \tag{2}$$

In Eq. (2), $[N^2, L_zS_z]_+$ denotes the anticommutator of $\mathbf{N}$ and the spin–orbit operators. The Fermi contact and dipolar terms have been omitted from the model. The hyperfine parameter b_F is zero to a first approximation due to the nature of the $3d_{\pm1}/4p_{\pm1}(\pi)$ $A^2\Pi$ wavefunction. The hyperfine parameter c was found to be poorly determined and constrained to zero. A 32×32 matrix representation in a case $a_{\beta J}$, non-parity, basis set was constructed and numerically diagonalized to produce eigenvalues and eigenvectors.

A weighted non-linear least squares fitting program was written that used as input initial guesses of the parameters, and the observed line positions and quantum number assignments of the associated levels (given in the supplemental tables). All of the data was fit simultaneously. The relative weights used for LIF data were 10 times higher than those of Fourier transform data. Preliminary fitting of the FT data, which has fewer branches due to the higher rotational levels observed, greatly assisted in formulating the final model. Since the FT data generally lacked hyperfine structure, judicious choice of final F'–F'' quantum number assignments for these data were necessary. Each rotational branch was treated individually by first extrapolating the initial LIF data model to higher branch features and calculating the relative intensities of the hyperfine

components at an elevated temperature of 1000 K to simulate the FT data. The most intense calculated component was selected and correspondingly used for each feature of each rotational branch.

The spectroscopic parameters used to fit the $A^2\Pi$–$X^2\Sigma^+$ and $B^2\Sigma^+$–$X^2\Sigma^+$ transitions are listed in Table 1. The $(0,0)$ and $(1,0)$ bands of the $B^2\Sigma^+$–$X^2\Sigma^+$ transitions have both LIF and FT measurements, and seven constants were considered for each state: B, D, γ, γ_D, b_F, c, and eq_0Q. The γ_D parameter for the $X^2\Sigma^+$ $(v = 0)$ state and the eq_0Q parameter for the $B^2\Sigma^+$ $(v = 0)$ and $B^2\Sigma^+$ $(v = 1)$ states were poorly determined and in the final fit were constrained to zero. The b_F and c parameters for the $B^2\Sigma^+$ $(v = 2$ and $3)$ states and the γ, c, and eq_0Q parameters for the $X^2\Sigma^+$ $(v = 1)$ state were constrained to values determined for the $B^2\Sigma^+$ $(v = 1)$ and $X^2\Sigma^+$ $(v = 0)$ states, respectively, because only FT data for the $B^2\Sigma^+$–$X^2\Sigma^+$ $(0,1)$, $(2,0)$, and $(3,1)$ bands were available. For the $A^2\Pi$ $(v = 1)$ state, nine parameters were determinable because the data set contained LIF measurements for both sub-bands and FT data for the $A^2\Pi_{3/2}$–$X^2\Sigma^+$

sub-band. The A, A_D, $p + 2q$, a, and d parameters for the $A^2\Pi$ $(v = 0)$ state were held fixed to those determined for the $A^2\Pi$ $(v = 1)$ state because only FT measurements for the $A^2\Pi_{3/2}$–$X^2\Sigma^+$ $(0,0)$ sub-band were available. Table 1 lists all of the parameters used in the final fit, along with the associated errors.

Simulation of the spectra was particularly useful. To do so either a 32×16 or 16×16 case $a_{\beta J}$ electric dipole transition probability matrix (*Tmat*) [18] for the $A^2\Pi$–$X^2\Sigma^+$ or $B^2\Sigma^+$–$X^2\Sigma^+$ band systems, respectively, was constructed. The transition moment (TM) was obtained by cross-multiplication of the transition probability matrix by the *case* $a_{\beta J}$ eigenvectors (*ev*) for the $X^2\Sigma^+$ and case $a_{\beta J}$ eigenvectors for either the $A^2\Pi$ or the $B^2\Sigma^+$ vibronic states. The equation used was

$$\text{TM} = ev(X^2\Sigma^+) \cdot TMat \cdot ev(A^2\Pi \text{ or } B^2\Sigma^+). \qquad (3)$$

The transition moment was squared, multiplied by a Boltzmann factor commensurate with a temperature of 40 K, and a Lorentzian lineshape (30 MHz FWHM) was

Table 1
The determined spectroscopic parameters[a] from the analysis of the $A^2\Pi$–$X^2\Sigma^+$ and $B^2\Sigma^+$–$X^2\Sigma^+$ transition wavenumbers

$X^2\Sigma^+$ parameters	$(v = 0)$ value[b]	$(v = 1)$ value[b]	$X^2\Sigma^+$ Eq. parameters	Value[b]
B	0.1972941(44)	0.1964867(44)	B_e	0.197698(7)
D	$0.9651(26) \times 10^{-7}$	$0.9696(26) \times 10^{-7}$	α_e	$8.07(6) \times 10^{-4}$
γ	0.003095(25)	0.003095[c]	R_e (Å)	2.13531(4)
b_F	0.055837(69)	0.05775(45)		
c	0.00388(46)	0.00388[c]		
eq_0Q	0.0021(18)	0.0021[c]		
$A^2\Pi$ parameters	$(v = 0)$ value[b]	$(v = 1)$ value[b]	$A^2\Pi$ Eq. parameters	Value[b]
A	111.7196[d]	111.7196(4)	B_e	0.184910(6)
A_D	-0.000092[d]	$-0.000092(3)$	α_e	$8.48(6) \times 10^{-4}$
B	0.184486(4)	0.183638(4)	R_e (Å)	2.20791(4)
D	$1.067(3) \times 10^{-7}$	$1.083(5) \times 10^{-7}$		
$p + 2q$	-0.05744[d]	$-0.05744(7)$		
q	$-0.000102(1)$	$-0.000212(6)$		
a	0.0056[d]	0.0056(3)		
d	0.0070[d]	0.0070(2)		
$B^2\Sigma^+$ parameters	$(v = 0)$ value[b]	$(v = 1)$ value[b]	$(v = 2)$ value[b]	$(v = 3)$ value[b]
B	0.1855831(44)	0.1846539(44)	0.1837183(46)	0.182773(5)
D	$1.0820(27) \times 10^{-7}$	$1.0878(26) \times 10^{-7}$	$1.0974(31) \times 10^{-7}$	$1.103(3) \times 10^{-7}$
γ	$-0.059904(37)$	$-0.059203(44)$	$-0.058732(86)$	$-0.05834(8)$
γ_D	$1.009(32) \times 10^{-7}$	$0.928(35) \times 10^{-7}$	$0.96(16) \times 10^{-7}$	$0.76(11) \times 10^{-7}$
b_F	0.00264(55)	0.00286(52)	0.00286[e]	0.00286[e]
c	0.0048(14)	0.0050(14)	0.00520[e]	0.00520[e]

$B^2\Sigma^+$ Eq. parameters	Value[b]	Band origins($T_{v'v''}$)	Value[b]
ω_e	488.737(5)	T_{00} A–X	11090.3959(16)
$\omega_e x_e$	2.06(4)	T_{01} A–X	10528.7874(17)
B_e	0.186055(6)	T_{10} A–X	11571.42190(22)
α_e	$9.37(3) \times 10^{-4}$	T_{00} B–X	12455.77376(39)
R_e(Å)	2.20111(4)	T_{10} B–X	12940.39815(34)
		T_{20} B–X	13420.9097(25)
		T_{01} B–X	11894.1511(20)
rms of fit = 0.0100		T_{31} B–X	13335.6308(23)

[a] All units in wavenumbers (cm^{-1}) unless indicated otherwise.
[b] Numbers in parentheses represent a 2σ error estimate in the last quoted decimal point.
[c] Value fixed to $X^2\Sigma^+$ $(v = 0)$ value.
[d] Value fixed to $A^2\Pi$ $(v = 1)$ value.
[e] Value fixed to $B^2\Sigma^+$ $(v = 1)$ value.

used for each spectral feature. This intensity calculation correctly predicts the diminishing intensities of specific G-doublet transitions at high temperatures mentioned earlier.

5. Discussion

Given the resolutions of the two experimental techniques and the large data set, the root mean square of the residuals of the fit (0.010 cm^{-1}) and the errors of the optimized parameters are quite reasonable and support the validity of our effective Hamiltonian model. A comparison of the newly determined parameters to the previously

determined parameters for the $B^2\Sigma^+$ ($v = 1$) and $X^2\Sigma^+$ ($v = 0$) states derived from the analysis of the $B^2\Sigma^+$–$X^2\Sigma^+$ (1, 0) band [7] is given in Table 2. The two sets of parameters are in reasonably good agreement and the differences can be attributed to the improved wavenumber determination and the re-assignment of some of the weaker features. Also presented in Table 2 is a comparison of the ScS spectroscopic parameters with those for $X^2\Sigma^+$ [14,19], $A^2\Pi$ [14,20] and $B^2\Sigma^+$ [21] states of ScO.

An interpretation of the fine and hyperfine parameters for the $X^2\Sigma^+$ ($v = 0$) and $B^2\Sigma^+$ ($v = 1$) states of ScS and comparison with isovalent ScO and ScNH [22] has been given previously [7]. The origins of the $A^2\Pi$–$X^2\Sigma^+$ and

Table 2
A comparison of the spectroscopic parameters for ScS and ScO

State	Parameters[a]	ScS[b]	ScS[c]	ScS[d]	ScO
$X^2\Sigma^+$ ($v = 0$)	B	0.1972941(44)	0.1961(3)	0.1971(3)	0.51346(5)[e]
	D	0.9651(26) $\times 10^{-7}$	—	5(5) $\times 10^{-8}$	0.590(10) $\times 10^{-6\,e}$
	γ	0.003095(25)	0.0032(2)	3(2) $\times 10^{-3}$	1.07324(13) $\times 10^{-4\,f}$
	b_F	0.055837(69)	0.0543(5)	0.06(3)	0.064128831(33)[f]
	c	0.00388(46)	0.0033(2)	—	0.002485521(67)[f]
	eq_0Q	0.0021(18)	0.0019(6)	—	0.00240967(17)[f]
	r_v (Å)	2.13750(2)	2.144(2)	2.139(2)	1.66780(8)[e]
$B^2\Sigma^+$ ($v = 1$)	T_{10}	12940.39815(34)	12940.3906(15)		
	B	0.1846539(44)	0.1842(2)		
	D	1.0878(26) $\times 10^{-7}$	—		
	γ	−0.059203(44)	−0.0581(8)		
	γ_D	0.928(35) $\times 10^{-7}$	—		
	b_F	0.00286(52)	0.0031(1)		
	c	0.0050(14)	0.0052(1)		
	eq_0Q	—	0.0032(7)		
	r_v (Å)	2.20944(3)	2.212(1)		
$B^2\Sigma^+$ ($v = 0$)	T_{00}	12455.77376(39)		12455.75(5)	20571.15(2)[g]
	B	0.1855831(44)		0.1853(1)	0.48308(5)[g]
	D	1.0820(27) $\times 10^{-7}$		6(2) $\times 10^{-8}$	0.674(5) $\times 10^{-6\,g}$
	γ	−0.059904(37)		−0.0594(6)	−0.0670(2)[g]
	γ_D	1.009(32) $\times 10^{-7}$		—	—
	b_F	0.00264(55)		—	—
	c	0.0048(14)		—	—
	eq_0Q	—		—	—
	r_v (Å)	2.20391(3)		2.2056(6)	1.71944(9)[g]
$A^2\Pi$ ($v = 0$)	T_{00}	11090.3959(16)			16498.13(2)[e]
	A	111.7196[i]			115.33(1)[e]
	A_D	−0.92 $\times 10^{-4\,i}$			8.9(1.0) $\times 10^{-5\,e}$
	B	0.184486(4)			0.50277(2)[e]
	D	1.067(3) $\times 10^{-7}$			0.654(10) $\times 10^{-6\,e}$
	$p+2q$	−0.05744[i]			−0.0661(5)[e]
	q	−0.000102(1)			−0.00032(3)[e]
	a	0.0056[i]			0.00450(3)[h]
	d	0.0070[i]			0.00590(7)[h]
	r_v (Å)	2.21045(2)			1.68544(3)[e]

[a] All units in wavenumbers (cm^{-1}) unless indicated otherwise.
[b] Present study.
[c] Ref. [7].
[d] Ref. [6].
[e] Ref. [14].
[f] Ref. [19].
[g] Ref. [21].
[h] Ref. [20], for the $A^2\Pi$ ($v = 1$) state.
[i] Fixed value from Table 1.

$B^2\Sigma^+$–$X^2\Sigma^+$ band systems of ScS are significantly red-shifted and much closer together than for ScO. These differences can be attributed to the higher ionization potentials of O (13.61 eV) vs. S (10.36 eV) and weaker ligand field effect of the S vs. O. The band origins of Table 1 produce $\Delta G_{1/2}$ ($X^2\Sigma^+$), $\Delta G_{1/2}$ ($A^2\Pi$), $\Delta G_{1/2}$ ($B^2\Sigma^+$), and $\Delta G_{3/2}$ ($B^2\Sigma^+$) values (in cm^{-1}) of 561.623, 481.026, 484.624, and 480.511, respectively. The $\Delta G_{1/2}$ ($B^2\Sigma^+$) and $\Delta G_{3/2}$ ($B^2\Sigma^+$) values are combined to produce $\omega_e = 488.737(5)$ cm^{-1} and $\omega_e x_e = 2.06(4)$ cm^{-1} for the $B^2\Sigma^+$ state. The rotational constants of Table 1 produce B_e, α_e, and R_e values for all three electronic states analyzed and are listed therein.

As mentioned in the introduction, the determined molecular parameters reveal parallels with those of the isovalent species ScO. The Λ-doubling parameters in the $A^2\Pi$ state are of the same magnitude and sign as for ScO, and their relationship to the spin-rotation parameter of the $B^2\Sigma^+$ state (e.g., $p_v A^2\Pi \approx \gamma_v B^2\Sigma^+$) strongly suggests a pure precession relationship of these states for both molecules. The hyperfine parameters a ($=0.00450(4)$ cm^{-1}) [20] and d ($=0.00590(8)$ cm^{-1}) [20] for the $A^2\Pi$ ($v = 1$) state of ScO are of the same magnitude and sign as those determined for ScS. Conversely, the spin-orbit centrifugal distortion parameter, A_D, for the $A^2\Pi$ state is of the same order of magnitude but has the opposite sign for ScS compared to ScO. The negative value determined in this work is consistent with a negative value determined for the $\tilde{A}^2\Pi$ state of the isoelectronic molecule ScNH [22].

It is reasonable to assume that the localized perturbations in the F_1 spin–rotation components for the $N = 4$ and $N = 5$ rotational levels of the $B^2\Sigma^+$ ($v = 1$) state arise from spin-orbit and rotational mixing with an excited vibrational level of the $A^2\Pi$ state. Using the $\Delta G_{1/2}$ ($A^2\Pi$) value, the fine structure parameters for $A^2\Pi$ ($v = 1$) state, and assuming that $\omega_e x_e$ ($A^2\Pi$) $= \omega_e x_e$ ($B^2\Sigma^+$) then the $J = 4.5$ and $J = 5.5$ levels of the $A^2\Pi_{1/2}$ ($v = 4$) spin–orbit component are predicted to be within a few wavenumbers of the perturbed $B^2\Sigma^+$ ($v = 1$) levels. The perturbed F_1 levels have e-parity. Accordingly, the perturbing $A^2\Pi_{1/2}$ ($v = 4$) levels also have to be e-parity and have identical J values [23]. The latter selection rule ($\Delta J = 0$) explains any lack of perturbations in the corresponding f-parity levels since each Λ-doublet of any N-level in the $A^2\Pi_{1/2}$ ($v = 4$) state has the same J value. The $N = 4$, e-parity level is pushed up by ~ 0.010 cm^{-1} whereas the $N = 5$, e-parity level is pushed down by ~ 0.003 cm^{-1}. Evidently, the e-parity Λ-doublet of the $J = 4.5$ level of the $A^2\Pi_{1/2}$ ($v = 4$) state lies just below the $N = 4$, e-parity level of the $B^2\Sigma^+$ ($v = 1$) state, whereas the e-parity Λ-doublet of the $J = 5.5$ level of the $A^2\Pi_{1/2}$ ($v = 4$) state lies at somewhat larger energy above the e-parity component of the $N = 5$ level of the $B^2\Sigma^+$ ($v = 1$) state. This is consistent with the determined fine structure parameters for the $B^2\Sigma^+$ ($v = 1$) state and those estimated for the $A^2\Pi_{1/2}$ ($v = 4$) state which predicts the splitting

between the $N = 4$ and $N = 5$, e-parity levels of the $B^2\Sigma^+$ ($v = 1$) state to be 1.85 cm^{-1} and the spacing between the $J = 4.5$ and $J = 5.5$ e-parity levels of the $A^2\Pi_{1/2}$ ($v = 4$) state to be 2.07 cm^{-1}.

The combined fit of FT measurements and LIF measurements has provided a much improved set of spectroscopic constants for the $X^2\Sigma^+$, $A^2\Pi$, and $B^2\Sigma^+$ states of ScS. In particular, the observation of high N rotational lines from the high temperature furnace has greatly improved the centrifugal distortion constants for the observed states. The fact that $B^2\Sigma^+$ state lies above the $A^2\Pi$ state and that they are interacting in a pure precession relationship leads to the negative sign of the Λ-doubling constant p_v of the $A^2\Pi$ state and of the spin constant γ_v of the $B^2\Sigma^+$ state as can be seen in Table 1.

Recently Andersson et al. [24] have reported the high-resolution analysis of the furnace spectra of the isovalent LaS molecule recorded using an FT spectrometer. In addition to the $A^2\Pi_r$–$X^2\Sigma^+$ and $B^2\Sigma^+$–$X^2\Sigma^+$ transitions, they observed an additional transition, $A^2\Pi_r$–$A'\,^2\Delta_r$ with the $A'\,^2\Delta_r$ state lying at about ~ 5000 cm^{-1} above the ground state. Based on the strong similarity between LaS and ScS we also expect a similar transition for ScS near 5000 cm^{-1}. So far we have not seen this transition in our FT scans below 10 000 cm^{-1}, probably due to weak intensity. More experiments are necessary to record improved spectra of ScS at longer wavelengths.

6. Conclusions

Eight vibrational bands have been recorded and modeled for the $A^2\Pi$–$X^2\Sigma^+$ and $B^2\Sigma^+$–$X^2\Sigma^+$ systems of ScS. For the $A^2\Pi$–$X^2\Sigma^+$ (1,0) band, the hyperfine structure was resolved and analyzed. We have reported the first observation/analysis of the $A^2\Pi$–$X^2\Sigma^+$ (0,1) band. The (0,1), (2,0), and (3,0) vibrational bands in the $B^2\Sigma^+$–$X^2\Sigma^+$ system have also been rotationally analyzed for the first time. Our analysis provides improved spectroscopic constants for comparison with those of the isovalent ScO molecule. For the $B^2\Sigma^+$–$X^2\Sigma^+$ (1,0) band perturbations were observed and tentatively assigned to an interaction between $v = 1$ of the $B^2\Sigma^+$ state and $v = 4$ of the $A^2\Pi_{1/2}$ spin component.

Appendix A. Supplementary data

Supplementary data for this article are available on ScienceDirect (www.sciencedirect.com) and as part of the Ohio State University Molecular Spectroscopy Archives (http://msa.lib.ohio-state.edu/jmsa_hp.htm).

References

[1] S.F. Rice, W.J. Childs, R.W. Field, J. Mol. Spectrosc. 133 (1989) 22–35.
[2] A.J. Bridgeman, J. Rothery, Dalton 2 (2000) 211–218.
[3] J. Jonnson, O. Launila, B. Lindgren, Mon. Not. R. Astron. Soc. 258 (1992) 49.
[4] J. Jonsson, B. Lindgren, A.G. Taklif, Astron. Astrophys. 246 (1991) L67–L68.
[5] R. Stringat, B. Fenot, Can. J. Phys. 54 (1976) 2293–2294.
[6] B. Fenot, J.L. Féménias, R. Stringat, J. Mol. Spectrosc. 78 (1979) 40–50.
[7] T.C. Steimle, A.J. Marr, D.M. Goodridge, J. Chem. Phys. 107 (24) (1997) 10406–10414.
[8] R.S. Ram, P.F. Bernath, M. Dulick, L. Wallace, Astrophys. J. Suppl. Ser. 122 (1999) 331–353.
[9] S. Gerstenkorn, P. Luc, Atlas du spectre d'absorption de la molécule de l'iode (Editions du C.N.R.S.) (1978); Rev. Phys. Appl. 14, 791 (1979).
[10] B.A. Palmer, R.A Keller, R. Engleman, Jr., An Atlas of Uranium Emission Intensities in a Hollow Cathode Discharge, Rough Draft of LASL Rep. LA-8251-MS (Los Alamos Scientific Laboratory, Los Alamos, N.M., 1980).
[11] C.J. Sansonetti, K.-H. Weber, Opt. Soc. Am. B 1 (3) (1984) 361–365.
[12] T.C. Steimle, J. Gengler, J. Chen, Can. J. Chem. 82 (6) (2004) 779–790.
[13] I. Mills, T. Cvitaš, K. Homann, N. Kallay, K. Kuchitsu, Quantities, Units, and Symbols in Physical Chemistry, second ed., Blackwell Scientific Publications, Oxford, 1993.
[14] R. Stringat, C. Athénour, J.L. Féménias, Can. J. Phys. 50 (1972) 395.
[15] G. Herzberg, Spectra of Diatomic Molecules, second ed. reprint w/corrections (Krieger Publishing, Malabar, FL 1989).
[16] Supplementary data for this article are available on ScienceDirect (www.sciencedirect.com).
[17] T.C. Steimle, W. Virgo, J. Chem. Phys. 116 (2002) 6012–6020.
[18] J.M. Brown, A. Carrington, Rotational Spectroscopy of Diatomic Molecules, Cambridge University Press, Cambridge, 2003.
[19] W.J. Childs, T.C. Steimle, J. Chem. Phys. 88 (1988) 6168.
[20] J. Shirley, C. Scurlock, T.C. Steimle, J. Chem. Phys. 93 (1990).
[21] A. Adam, W. Klemperer, T.M. Dunn, Can. J. Phys. 46 (1968) 2213.
[22] T.C. Steimle, J. Xin, A.J. Marr, S. Beaton, J. Chem. Phys. 106 (1997) 9084.
[23] H. Lefebvre-Brion, R.W. Field, Perturbations in the Spectra of Diatomic Molecules, Academic Press, London, 1986.
[24] N. Andersson, S.P. Davis, G. Edvinsson, R.J. Winkel, Phys. Scr. 64 (2001) 134–139.